Experimental investigations of fracture process in concrete by means of x-ray micro-computed tomography

Ł. Skarżyński and J. Tejchman
Faculty of Civil and Environmental Engineering
Gdańsk University of Technology, Poland
lskarzyn@pg.gda.pl, tejchmk@pg.gda.pl

Abstract

The paper describes investigation results on fracture in notched concrete beams under quasi-static three-point bending by the x-ray micro-computed tomography. The 2D and 3D image procedure was used. Attention was paid to width, length, height and shape of cracks along beam depth. In addition, the displacements on the surface of concrete beams during deformation process were measured with the digital image correlation (DIC) technique in order to detect strain localization before a discrete crack occurred. The fracture 2D pattern in a beam was numerically simulated with FEM using an isotropic damage constitutive model enhanced by a characteristic length of micro-structure. Concrete was modelled as a random heterogeneous 4-phase material composed of aggregate, cement matrix, interfacial transitional zones (ITZs) and air voids. The advantages of the x-ray micro-computed tomography were outlined.

Keywords: x-ray micro-CT, concrete, DIC, crack, fracture, microstructure, strain localization, FEM

1. Introduction

Fracture is a fundamental phenomenon in concrete materials. It is very complex since it consists of main cracks with various branches, secondary cracks and micro-cracks [1]. During fracture, micro-cracks first arise in a hardening region on the stress-strain curve which change gradually during material softening into dominant distinct macroscopic cracks up to damage. Thus, a mechanical fracture process is generally subdivided into two main stages: 1) the appearance of narrow regions of intense deformation (equivalent to the region of intense micro-cracking called fracture process zones FPZs) ahead of macro-cracks and 2) the occurrence of discrete macro-cracks [2]. A realistic description of fracture process zone (FPZ) in concrete (their width, length, shape and distance) is very important since they are not negligibly small as compared to the specimen size and are large

enough to cause significant stress redistribution in the structure and associated energy release contributing to a size effect [1]. The fracture process strongly depends upon a heterogeneous structure of materials over many different length scales, changing e.g. in concrete from the few nanometres (hydrated cement) to the millimetres (aggregate particles). In order to properly describe fracture process, a material micro-structure has to be taken into account which effect on the global results is pronounced. At the meso-scale, concrete may be considered as a composite material by distinguishing 4 important phases: aggregate, cement matrix, interfacial transition zones ITZs (contact zones between the cement matrix and aggregate) and macro voids [3-6]. In particular, the presence of aggregate particles and ITZs is important since the volume fraction of aggregate can be as high as 70-75% in concrete and the ITZs with the thickness of about 50 μm are always the weakest region in usual concretes (wherein cracking starts because of their higher porosity) [4]. A direct observation of fracture is difficult because of a small scale at which micro-structural events interact with a failure process. Different techniques have been used to experimentally investigate fracture in quasi-brittle materials (concrete, rock and masonry) at the laboratory scale such as: scanning electron microscopy (SEM) [7-9], high speed photography [10], laser speckle interferometry [11, 12], acoustic emission [13-15], X-ray technique [16-18], moiré interferometry [19, 20] and digital image correlation technique [21-26]. One of the most popular methods (due to its availability, simplicity and low cost) is the DIC technique, wherein material displacements are obtained by tracking a random speckle pattern applied to the surface by means of digital images at different instances of deformation. Next strains, which are the best indicator for localized zones, are calculated, based on displacements, using standard finite-element shape functions. The method gives high resolution measurements of a displacement field. It can be used both for 2D and 3D measurements. For concrete, strain localization and cracks can be both easily identified that are certainly two key parameters needed to estimate the permeability, strength and durability of structural concrete components [1, 2]. This method has two serious drawbacks: no information about material microstructure and fracture inside the material may be achieved. Recently, the application of the high-resolution x-ray tomography (called also micro–computed tomography, micro-CT or μCT) significantly increased. It is a non-destructive technique that provides 3D images of the internal structure in materials from different life domains [27-31]. The image analysis offers the possibility to study in detail the size and shape of each individual particle present in granular and cementitious materials.

The main objective of this experimental study is to investigate fracture in concrete elements under bending using micro-tomography by taking the concrete micro-structure into account. The experiments were conducted to better understand a fracture process phenomenon in quasi-brittle

materials and to enable the calibration of our mesoscopic continuum and discrete models for the description of the concrete behaviour [32-37]. Next, some numerical 2D calculations at the aggregate level were carried out with the measured micro-structure. The numerical simulations were carried out with a simple isotropic continuum constitutive damage model [33, 34] enhanced by a characteristic length of micro-structure by means of a non-local theory [38-40]. Concrete beam was assumed at meso-scale as a random heterogeneous material composed of 4 phases: aggregate, cement matrix, interfacial transition zones (ITZs) and macro air voids. The major contribution of the paper is: 1) 3D images of micro-structure of concrete beams before and after the damage and 2) numerical 2D calculations of fracture with the measured concrete micro-structure.

2. X-ray micro-tomography

The x-ray micro-tomography (called micro-CT or μCT) is a non-destructive 3D imaging technique which uses x-rays to create cross-sections of a physical object that is used to recreate a virtual model (3D model) without destroying the original object (Figure 1). The pixel sizes of the cross-sections are in the micro-metre range. The first x-ray microtomography system was conceived and built by Jim Elliott in the early 1980s [41]. The basic physical x-ray principal of the computed tomography is the interaction of the ionizing radiation with the material, where the so-called photo-effect builds the main interaction mechanism. The photo-effect attenuates the photons proportional to the third power of the order number of the elements and inverse proportional to the third power of the photon energy. As the x-ray beam penetrates an object, it is exponentially attenuated according to the material along its path. The energy-dependent material constant appearing in the exponent of the attenuation formula is called the linear attenuation coefficient. It expresses the amount of the radiation that is attenuated on an infinitely small distance in which the final attenuation reflects the sum of all these local linear attenuations along the x-ray beam. The x-ray image represents an image of the sum of all local attenuations along the x-ray beam [42]. The 3D images of the interior of an object are obtained by collecting a series of 2D images that are stored while the specimen investigated is rotated. The internal structures are reconstructed using the combination of all 2D cross-sections (projections) which are then used to analyse the 2D or 3D morphological parameters of the object and create a realistic visual model. The source is mostly either a micro-focus x-ray tube or a device of a synchrotron radiation facility. The detector is normally based on a CCD camera with a phosphor layer to convert x-rays to a visible light.

Some artefacts are commonly encountered in computed tomography (CT) and may obscure or simulate pathology. There are many different types of CT artefacts, including: ring artefacts, noise,

beam hardening and scatter, motion artefact, misalignment, metal artefacts, out of field artefacts and defect pixels which were discussed in detail in [44, 45].

The x-ray micro-tomography technique has been already used to cementitious materials, mainly to mortars (with maximum aggregate size 2 mm) using small specimens. Internal cracking patterns in small mortar specimens were observed by Landis et al. [46-48]. The scanned specimen were very small in the form of cylinders 4 mm in diameter by 4 mm high and the maximum aggregate size was only 0.425 mm. The spatial resolution was equal to 9.6 microns. In the tests by Lu et. al. [49] the pore structure of concrete was studied. The specimen size was $5\times6\times6$ mm^3 large and the spatial resolution was 1-4 microns. Burlion et. al. [50] dealt with leaching of cementitious materials. The micro-structure evolution in a standard mortar with the maximum grain size of 2 mm subjected to a chemical attack was analysed (the cylindrical cores of 8 mm diameter and length equal 20 and 30 mm). The spatial resolution was initially equal 4.9-7.5 microns. Promentilla and Sugiyama [51, 52] studied the internal structure of mortars which were exposed to the freezing-thawing action (cored cylindrical samples of 12 mm in diameter and 24 mm in height). The spatial resolution was in order of 12 microns. Lydzba et. al. [53] analysed the processes of concrete degradation caused by chemical processes. A cylindrical concrete specimen of the diameter of 5 cm and height 10 cm was used. The spatial resolution was equal 7-14 microns.

Our x-ray micro-tomograph Skyscan 1173 (Figure 2) represents a new generation in high-resolution desktop X-ray microtomography systems for scanning. It is particularly advantageous at intermediate resolution levels, where scans are completed up to ten times faster with the same resolution and image quality, compared to previous micro-CTs with a fixed source-detector design. It is equipped with the newly developed 130 keV microfocus x-ray source with a very stable focal spot position, flat panel sensor of a large format (5 Mpx) with a special protection by a lead-glass fibre-optic window. The table scanner is additionally equipped with a precision object manipulator which allows for a very precise and automatic specimen positioning. It has several filters available in the front of the x-ray detector: 0.25 mm brass filter, 1.0 aluminium filter, 2.0 mm lead filter and 0.25 copper filter. As compared to usual micro-tomographs, there are two main advantages of our apparatus: a) large specimens up to 300 mm in diameter may be scanned and b) the specimens are scanned with a higher precision (2-3 microns). During tests with concrete beams, the x-ray source voltage of the micro-CT scanner was set to 100 keV, the current to 78 μA and the exposure time to 1800 ms. The pixel size was 19.5 μm.

3. Specimen preparation and experimental set-up

3.1 Specimen preparation

The concrete was prepared from an ordinary Portland cement (CEM I 32.5 R), aggregate and water. The river sand and gravel (round-shaped) aggregate was used with the mean aggregate diameter d_{50}=2 mm, maximum aggregate diameter d_{max}=16 mm and aggregate volume of β=75%. The water to cement ratio was equal to 0.42 (Table 1). A small superplasticizer quantity was used to improve the workability of the fresh concrete. The tests were carried out on 2 free-supported rectangular notched concrete beams (height D=80 mm, depth B=40 mm and length L=320 mm). The notch of the height of D/10=8 mm and width of 3 mm was located at the mid-span (Figure 3). The beams were cut out from the same mix block after the 7th day which was covered with a plastic sheet during the initial curing period to avoid the surface evaporation and autogeneous shrinkage. The elements were next kept 28 days in water. The measured compressive strength f_c, Young's modulus E and Poisson's ratio υ were equal to: f_c=51.81 MPa, E=36.1 GPa and υ=0.22. Before tests, the concrete surface was carefully polished and painted white. Next a speckle pattern (serving as a tracer in DIC) was put on this surface using a black colour spray. The speckle pattern had approximately 10 pixels per black dot.

3.2 Experimental set-up

The quasi-static test with concrete beam was performed with a controlled notch opening displacement rate (or Crack Mouth Opening Displacement, CMOD) of 0.002 mm/min. This type of control allowed for obtaining a gradual increase in the crack opening and a steady strength decrease in a post-peak regime. A CMOD gauge with the length of 5 mm was located in the notch at the beam bottom. The gauge precision was 0.0025 mm at the maximum permissible axial displacement of 2 mm. The test ended for the CMOD≈0.1 mm.

The experimental program included 2 main steps. In the first step, the bending process was registered by means of the 2D micro-tomograph and 2D DIC technique. The displacement on the beam surface were measured by DIC [54, 55] using the digital camera Canon EOS-1Ds Mark II with the 16.7 megapixel CMOS sensor. The camera with the image size of 3546 pixels × 2304 pixels was fixed in a certain distance from the beam in order to provide the image with the area of about 110×70 mm^2. Thus, one pixel represented approximately the square of 60 μm on the beam surface and the length image resolution was 17 pixel/mm. The patch size was assumed to be bigger

at least by 1 pixel than the biggest speckle used, i.e. ≥30 pixels. The distance between the search patch centres was equal 5 pixels. The details of DIC measurements for concrete beams were described in [56].

In the second step, 2 concrete cuboids with the dimensions of 80 mm (height), 50 mm (width) and 40 mm (depth) were cut out from each beam after each test, using a diamond saw, for scanning by the x-ray micro-tomograph in order to obtain the 3D images. One specimen was cut out in a cracked area (in the notch region) and the second one in a non-cracked area (beyond the notch region). The x-ray source voltage of the micro-CT scanner was set to 130 keV, the current was 61 μA and exposure time was equal 5000 ms. The pixel size was 31.74 μm. The x-ray projections were recorded with the rotation increment of 0.2° within 360°. In order to reduce the noise in the X-ray projections, the frame averaging option was 6 and random movement option was 50. The scanning time was approximately 18 hours. The image reconstruction was carried out with the NRecon software.

4. Experimental results

Two experimental curves of the vertical force F versus CMOD for the concrete beams of Figure 3 (up to 0.16 mm for the beam '1' and up to 0.10 mm for the beam '2') are shown in Figure 4. The maximum vertical force F was equal to 2.15-2.25 kN (the tensile strength 3.73-3.91 MPa). Figure 5 presents two concrete 2D images obtained with the micro-tomograph which are the average image values obtained through the entire beam depth (concrete beam '2'). However, a localized zone above the notch at the peak load (Fig.5a) could not be clearly detected and a few cracks above the notch (instead of one) in the residual state were noticeable (Fig.5b).

The DIC technique was used in the concrete beam '1' (it could not be used together with the 2D microCT in the beam '2' for technical reasons). Based on the strain distribution in the beam (Figure 6), a localized zone was created before the peak on the vertical force-CMOD diagram for the about 90% of the peak force in the pre-peak regime (Figure 7). It appeared as a single strongly curved zone. The localized zone width rapidly developed during the CMOD displacement increment of 0.002 mm for CMOD=0.012 mm. Next it slightly decreased during a deformation process in the range of CMOD=0.014-0.06 until a discrete macro-crack formed (point '6' in Figure 7). The maximum horizontal strain was 0.01. The width and length of the localized zone were very similar on both sides of the beams, however, its shape was different. The maximum length and height of the localized zone above the notch were l_{lz}=65 mm and h_{lz}=55 mm (h_c/D≈0.68) for

CMOD≈0.05 mm. The measured surface displacements from DIC were fitted by the error function ERF whereas the surface strains calculated from the displacements were fitted by the usual normal distribution (Gauss) function [57]. A localized zone width above the notch was equal to w_{lz}=3.48 mm (1.74×d_{50}, 0.22×d_{max}) for CMOD≈0.05 mm. The width of a localized zone w_{lz} varied at the different height above the notch (e.g. w_{lz}=2.25 mm at h=55 mm and w_{lz}=3.87 mm at h=15 mm). The details of a localized zone in notched concrete beams were described in [56].

Figure 8 demonstrates the 3D image of the cracked and non-cracked cubical concrete specimens after the test. The specimen of Figure 8Aa was cut out from the beam '1' for CMOD≈0.16 mm when the beam was totally cracked along the height. The specimen of Figure 8Ba was cut out from the beam '2' for CMOD=0.1 mm. The 3 phases (aggregate particles, cement matrix and voids) are well seen in Figure 9. The crack location in the various vertical and horizontal cross-sections after the test is described in Figure 10 (CMOD=0.1 mm). Figure 11 presents the changes of the crack width in different vertical and horizontal cross-sections.

The heterogeneous concrete micro-structure is well visible (Figure 8) and the 3 phases (aggregate particles, cement matrix and air voids) can be distinguished (Figure 9). The shape of the crack varies along the beam depth (Figure 10). The crack width in the tensile region changes non-linearly with the specimen height (Figure 11A) from w_c=0.32 mm (above the notch) down to w_c=0.02 mm. The crack width above the notch also changes with the specimen depth from w_c=0.33 mm (at the depth of 5 mm from the face side, Figure 11Bc) down to w_c=0.13 mm (at the depth of 35 mm, Figure 11Ba). The average crack width in the specimen is 0.20 mm. The mean crack height is h_c=50 mm. The crack height changes along the specimen depth (from h_c=45 mm up to h_c=56 mm). On the front side h_c=56 cm>h_{lz}.

Table 2 provides the data on the length and area of the crack in the different horizontal and vertical cross-sections of Figure 10 (the average crack width is also given). The average crack surface area is equal 2418.5 mm^2 and the average crack length is 54.78 mm. The crack length changes within the specimen depth. The largest length is equal to 59.31 mm on the front beam side. The mean crack volume is 507.9 mm^3.

Figure 12 presents the 2D distribution of air voids in 3 different horizontal cross-sections above the beam notch in the cubical non-cracked and cracked concrete specimen of Figure 8B (at the height of 3 mm, 15 mm and 30 mm above the notch). In these horizontal cross-sections (without the crack), the void area is equal to 76.59 mm^2 (4.58% of the area of Figure 12Aa), 89.33 mm^2 (5.28% of the

area of Figure 12Ab) and 84.88 mm^2 (5.02% of the area of Figure 12Ac), respectively (Table 3). The total volume of the air voids is 5010.84 mm^3 (4.67% of the analyzed specimen volume). In the concrete specimen with the crack (Figure 12B), the void area is equal to 83.12 mm^2 (4.47% of the area of Figure 12Ba), 76.01 mm^2 (4.09% of the area of Figure 12Bb) and 103.96 mm^2 (5.60% of the area of Figure 12Bc). The total volume of the air voids is 6468.81 mm^3 (5.48% of the analyzed specimen volume), i.e. higher than in the non-cracked specimen (5010.84 mm^3).

The crack is strongly curved due to presence of aggregate grains and air voids. The crack solely propagated through the cement matrix and ITZs which were the weakest phase in concrete (concrete beam '2'). In the concrete specimen '2', the crack also propagated through a weak aggregate particle (Figure 13). In order to measure the width of ITZs, the scanning electron microscope (SEM) Hitachi TM3030 with the magnification factor 30'000 was used. The width of the ITZs changed between 30-50 μm (Figure 14).

5. Constitutive model for concrete

A simple isotropic damage continuum model was used [33, 54] which describes the material degradation with the aid of only a single scalar damage parameter D growing monotonically from zero (undamaged material) to one (completely damaged material). A damage variable D is associated with a degradation of the material due to the propagation and coalescence of micro-cracks and micro-voids. It is defined as the ratio between the damage area and the overall material area. The stress-strain relationship is represented by

$$\sigma_{ij} = (1-D)C^{e}_{ijkl}\varepsilon_{kl}, \tag{1}$$

where C^{e}_{ijkl} is the linear elastic material stiffness matrix (including modulus of elasticity E and Poisson's ratio υ) and ε_{kl} is the strain tensor. The damage parameter D acts as a stiffness reduction factor (the Poisson's ratio is not affected by damage) that changes from 0 to 1. The growth of damage is controlled by the damage threshold parameter κ which is defined as the maximum equivalent strain measure $\tilde{\varepsilon}$ reached during the load history up to time t. The loading function of damage is

$$f(\tilde{\varepsilon},\kappa) = \tilde{\varepsilon} - \max\{\kappa,\kappa_0\}, \tag{2}$$

where κ_0 denotes the initial value of κ when damage begins. If the loading function f is negative, damage does not develop. During monotonic loading, the parameter κ grows (it coincides with $\tilde{\varepsilon}$) and during unloading and reloading it remains constant. To define the equivalent strain measure $\tilde{\varepsilon}$, a Rankine failure type criterion was assumed [57]

$$\tilde{\varepsilon} = \frac{1}{E} \max\left\{\sigma_i^{eff}\right\}, \tag{3}$$

where E is the modulus of elasticity and σ_i^{eff} are the principal values of the effective stress

$$\sigma_i^{eff} = \sigma_{ijkl}^{e} \varepsilon_{kl}. \tag{4}$$

To describe the evolution of the damage parameter D, the exponential softening law was used [58]

$$D = 1 - \frac{\kappa_0}{\kappa}\left(1 - \alpha + \alpha e^{-\beta(\kappa - \kappa_0)}\right), \tag{5}$$

where α and β are the material constants. The constitutive isotropic damage model for concrete requires the following 5 constants: E - the elastic modulus, υ - the Poisson's ratio, κ_0 - the initial value of the damage parameter and α and β - the softening parameters. The model is suitable for tensile failure [34]. However, it cannot realistically describe irreversible deformations, volume changes and shear failure.

To properly describe strain localization, to preserve the well-possedness of the boundary value problem and to obtain mesh-independent results, a non-local theory was used as a regularization technique [1, 59]. In this theory, the principle of a local action does not take place any more. In the calculations, the equivalent strain measure $\tilde{\varepsilon}$ was replaced by its non-local value [33]

$$\overline{\varepsilon} = \frac{\int_V \omega\left(\|x - \xi\|\right)\tilde{\varepsilon}\left(\xi\right) d\xi}{\int_V \omega\left(\|x - \xi\|\right) d\xi}, \tag{6}$$

where V - the body volume, x - the coordinates of the considered material point, ξ - the coordinates of surrounding points and ω - the weighting function. The equivalent strain measure $\tilde{\varepsilon}$ near

boundaries was calculated also on the basis of Eq.3.6 (which satisfies the normalizing condition). As a weighting function ω, a Gauss distribution function was used

$$\omega(r) = \frac{1}{l_c\sqrt{\pi}} e^{-\left(\frac{r}{l_c}\right)^2}, \tag{7}$$

where l_c denotes a characteristic length of micro-structure and the parameter r is a distance between two material points. The averaging in Eq.7 is restricted to a small representative area around each material point (the influence of points at the distance of $r=3\times l_c$ is only 0.01%). A characteristic length is usually related to material micro-structure and is determined with an inverse identification process of experimental data [60]. The characteristic length was always assumed l_c^m=1.5 mm based on experiments [33, 55] (where l_c^m denotes the mesoscopic characteristic length and is related to material micro-structure).

The 2D calculations were performed only. The location, shape, size and distribution of aggregate grains and air voids were directly taken from the microstructure at the depth of 3 mm from the front of the concrete beam surface in the notch region (Figure 15). The FE mesh for the entire notched concrete beam '2' is shown in Figure 16. The FE-mesh included in total approximately 100'000 triangular elements. The width of the meso-region was equal to 50 mm and was equal to the width of the cuboid (cut out from the beam). This width of the assumed meso-region was sufficient since the localized zone propagated in a heterogeneous beam part far from a homogeneous one [33]. Concrete was treated in the meso-scale region close to the notch as a random four-phase heterogeneous material with angularly-shaped aggregate particles using material constants in Table 4. In the remaining region, the material was the elastic one-phase material (E_{macro}=36.1 MPa and υ_{macro}=0.2).

The modulus of elasticity of the aggregate grains (composed of 55% of granite, 30% of limestone, 13% of sandstone and 2% of basalt) was calculated as the mean value of the module of the components [61]

$$\begin{aligned} E_{aggr} &= 0.55E_g + 0.30E_l + 0.13E_s + 0.02E_b = \\ &= 0.55\times 75 + 0.30\times 6 + 0.13\times 20 + 0.02\times 80 = 47.2\,\text{GPa} \end{aligned} \tag{7}$$

The modulus of elasticity of the cement matrix was assumed as E_{cm}=29.2 GPa based on own tests. The interfacial transition zone (ITZ) is a special region of the cement paste around particles which is perturbed by their presence [62-64]. Its origin lies in the packing of the cement grains against the much larger aggregate which leads to a local increase in porosity (micro-voids) and a presence of smaller cement particles. A paste with the lower *w/c* (higher packing density) or made from finer cement particles leads to ITZ of a smaller extent. This layer is highly heterogeneous and damaged and thus critical for the concrete behaviour. According to Königsberger et al. [64], two different types of failure exist for ITZs: the ITZ-aggregate separation (related to some delamination processes directly at the aggregate surface) and the ITZ-failure (related to cracking). An accurate understanding of the properties and behaviour of ITZ is one of the most important issues in the meso-scale analyses because damage is initiated at the weakest region and ITZ is just this weakest link in concrete. The width of bond zones (ITZs) surrounding each aggregate grain was assumed to be constant and equal to 50 μm (the maximum value from measurements using SEM, Figure 14). We assumed that ITZs had the reduced stiffness and strength as compared to the cement matrix (in the proportion of 50%) (Table 4). The parameters κ_0, α and β in (Table 4) were adjusted to fit the shape of the experimental curves of Figure 4. The size of finite elements was 0.025-0.2 mm (aggregate), 0.025-0.2 mm (cement matrix) and 0.025 mm (ITZs) (Figure 15). The air voids (2.5% of the total area, with the diameter ≥ 0.8 mm) were modelled as the empty spots.

6. Numerical results for meso-scale 2D approach

Figure 17 demonstrates the load-CMOD curve obtained for the concrete beam '2' with the real aggregate and air voids distribution (at the depth of 3 mm from the beam front side) in the notch region obtained by micro-CT (E^{ITZ}=14.6 GPa, κ_0^{ITZ}=1.1×10^{-5}, l_c^m=1.5 mm). The calculated and experimental force-CMOD curves are the same in an entire elastic regime and very similar in the softening regime. The maximum vertical force F from the experiments was equal 2.25 kN for CMOD=0.016 mm and from the FE computations 2.29 kN for CMOD=0.017 mm. The shape, height and location of the localized zone from the FE computations is in satisfactory agreement with the experimental outcome (Figure 18). The localized zone propagates through ITZs only as in the experiment (beam '2'). The width and length of the localized zone are very similar as in the experiments of Figure 6. The maximum calculated length and height of the localized zone above the notch (beam '1') are l_{lz}=67 mm and h_{lz}=56 mm (h_{lz}/D≈0.70) for CMOD=0.1 mm. In the experiments with the beam '2', the crack length and height are: l_c=59 mm and h_c=52 mm (h_c/D≈0.65) for CMOD=0.1 mm. The calculated width of the localized zone width above the notch is w_c=3.82 mm

(w_c=3.48 mm in the experiments with the beam '1') for CMOD=0.05 mm. It changes along the beam height. Its largest width is w_{lz}=4.5 mm ($3\times l_c^m$ for h=30 mm). In the experiments with the beam '1', the largest width of the localized zone was 3.87 mm for h=15 mm.

The effect of the ITZ stiffness on the numerical results is described in Figure 19. The stiffness E^{ITZ} was assumed to be equal to 25%-75% of the cement matrix stiffness. The crack initiation strain in ITZ was $\kappa_0=4.0\times10^{-5}$. Since ITZ is the weakest phase, the ultimate beam strength increased with its increasing stiffness (Figure 19A). The stiffness of ITZs strongly affected both the load-CMOD response and shape of the localized zone. The width of the localized zone changes was not affected. The shape of the force-CMOD curve and localized zone were not also influenced by the material constant $\kappa_0^{ITZ}=4.0\times10^{-5}$ - 1.1×10^{-4}. However, the strength was strongly affected (the larger κ_0^{ITZ}, the higher was the maximum and residual vertical force) (Fig.20).

7. Conclusions

The following conclusions can be drawn from quasi-static experiments on notched concrete beams under three-point bending:

- X-ray micro-CT is a powerful tool for the visualization of concrete micro-structure (aggregate, cement matrix, voids) and crack propagation.
- In the experiments, the crack shape changed along the beam depth (although plane loading problem was considered). The crack was strongly curved since it propagated through the weakest contact zones between the cement matrix and aggregate grains (ITZs). The width of ITZs varied between 30 and 50 μm. The crack sometimes propagated through a weak aggregate particle.
- The crack height varied in the experiments between 45-55 mm along the beam depth (the average height was 50 mm, $h_c/D\approx0.62$). The crack was 59.31 mm long near the front beam side; the average crack length was 54.8 mm. The crack width changed non-linearly with the specimen height from 0.32 mm down to 0.02 mm above the notch. The crack width also changed with the specimen depth from 0.13 mm up to 0.33 mm The average crack width in the specimen was 0.20 mm.
- The experimental average crack surface area was 2418.5 mm^2 and the mean crack volume was 507.9 mm^3.

- The width of the experimental localized zone on the beam front side above the notch was equal to w_{lz}=3.48 mm (1.74×d_{50}, 0.22×d_{max}). The width of the localized zone varied at the different height above the notch between 2.25-3.87 mm. The height of the localized zone on the front side above the notch was 41 mm for the maximum vertical force.
- The total volume of the air voids in concrete beam specimens was 4.7% (non-cracked specimen) and 5.5% (cracked specimen).

The material micro-structure on the meso-scale has to be taken into account in calculations of fracture to obtain a proper shape of cracks. The isotropic damage continuum model enhanced by a characteristic length of micro-structure properly captured the evolution of a localized zone above the beam notch under quasi-static three-point bending where concrete was treated as a heterogeneous four-phase material. The properties of ITZs had a huge influence on the material strength and shape of the localized zone and thus have to be carefully determined. Our experiments will be continued. The servo-testing machine INSTRON 5569 will be equipped with a special load handle which will allow for the concrete specimen rotation during deformation. The successive 3D images during beam deformation will be obtained soon.

Acknowledgements

The research work has been carried out within the project: "*Innovative ways and effective methods of safety improvement and durability of buildings and transport infrastructure in the sustainable development*" financed by the European Union (POIG.01.01.02-10-106/09-01) and the project "*Experimental and numerical analysis of coupled deterministic-statistical size effect in brittle materials*" financed by National Research Centre NCN (UMO-2013/09/B/ST8/03598).

References

[1] Bažant, Z. and Planas, J (1998) Fracture and size effect in concrete and other quasi-brittle materials. CRC Press LLC, Boca Raton.

[2] Nielsen, A. U., Montiero, P. J. M. and Gjorv, O. E. (1995) Estimation of the elastic moduli of lightweight aggregate, *Cement and Concrete Research* **25**, 276-280.

[3] Sengul, O., Tasdemir, C. and Tasdemir, M. A. (2002) Influence of aggregate type on mechanical behaviour of normal- and high-strength concretes, *ACI Materials Journal* **99**, 528-533, 2002.

[4] Lilliu, G. and van Mier, J. G. M. (2003) 3D lattice type fracture model for concrete. *Engineering Fracture Mechanics* **70**, 927-941.

[5] Kozicki, J. and Tejchman, J. (2008) Modelling of fracture processes in concrete using a novel lattice model. *Granular Matter* **10**, 377–388.

[6] He, H., Guo, Z., Stroeven, P., Stroeven, M. and Sluys, L. J. (2009) Influence of particle packing on elastic properties of concrete. *Proc. First International Conference on Computational Technologies in Concrete Structures (CTCS'09),* Jeju, Korea, 1177-1197.

[7] Nemati, K. M. (1997) Fracture analysis of concrete using scanning electron microscopy, *Scanning* **19**, 426-430.

[8] Balendran, R. V., Pang, H. W. and Wen, H. X. (1998) Use of scanning electron microscopy in concrete studies. *Structural Survey* **16**, 146-153.

[9] Hadjab, S. H, Chabaat, M., Thimus, J. F. (2007) Use of Scanning Electron microscope and the non-local isotropic damage model to investigate fracture process zone in notched concrete beams. *Experimental Mechanics* **47**, 473–84.

[10] Bhargava, J. and Rehnström A. (1975) High speed photography for fracture studies of concrete, *Cement and Concrete Research* **5**, 239-248.

[11] Leendertz, J. A. (1970) Interferometric displacementmeasurement on scattering surfaces utilizing speckle effect. *Journal of Physics E: Scientific Instruments* **3**, 214–218.

[12] Jacquot, P., and Fournier, J. M. (2000) Interferometry in Speckle Light: *Theory and Applications*. Springer, Berlin.

[13] Maji, A., Ouyang, C. and Shah, S. P. (1990) Fracture mechanisms of concrete based on acoustic emission. *Journal of Materials Research* **5**, 206-217.

[14] Mihashi, H. and Nomura, N. (1996) Correlation between characteristics of fracture process zone and tension-softening properties of concrete. *Nuclear Engineering and Design* **165**, 359-376.

[15] Carpinteri, A. and Lacidogna, G. (2003) Damage diagnostic in concrete and masonry structures by acoustic emission technique. *Automatic Control and Robotics* **3**, 755-764.

[16] Otsuka, K. and Date, H. (2000) Fracture process zone in concrete tension specimen. *Engineering Fracture Mechanics* **65**, 111-131.

[17] Hadjab, H. (2009) Fracture process zone in concrete beams: experimental investigation and numerical modelling. *Proceedings of the SEM Annual Conference*, June 1-4, Albuquerque New Mexico USA.

[18] Zhang, D. and Wu, K. (1999) Fracture process zone of notched three-point-bending beams. *Cement and Concrete Research* **29**, 1887-1892.

[19] Ri, S., Fujigaki, M. and Morimoto, Y. (2010) Sampling Moiré Method for Accurate Small Deformation Distribution Measurement. *Experimental Mechanics* **50**, 501-508.

[20] Ri, S., Muramatsu, T., Saka, M. Nanbara, K. and D. Kobayashi (2012) Accuracy of the Sampling Moiré Method and its Application to Deflection Measurements of Large-Scale Structures. *Experimental Mechanics* **52**, 331-340.

[21] Haidar, K., Pijauder-Cabot, G., Dube, J. F. and Loukili, A. (2005) Correlation between the internal length, the fracture process zone and size effect in model materials. *Materials and Structures* **38**, 201-210.

[22] Lecompte, D., Smits, A., Bossuyt, S., Sol, H., Vantomme, J., van Hemelrijck, D., Habraken, A. M. (2006) Quality assessment of speckle patterns for digital image correlation. *Optical and Lasers in Engineering* **44**, 1132-1145.

[23] Corr, G., Accardi, M., Graham-Brady, L. and Shah, S. (2007) Digital image correlation analysis of interfacial debonding properties and fracture behavior in concrete. *Engineering Fracture Mechanics* **74**, 109-121.

[24] Pan, B., Xie, H., Wang, Z., Qian, K. and Wang, Z. (2008) Study on subset size selection in digital image correlation for spackle patterns. *Optics Express* **16**, 7037-7048

[25] Wu, Z., Rong, H., Zheng, J. and Dong, W. (2011) An experimental investigation on the FPZ properties in concrete using digital image correlation technique. *Engineering Fracture Mechanics* **78**, 2978-2990.

[26] Alam, S. Y., Loukili, A. and Grondin, F. (2012) Monitoring size effect on crack opening in concrete by Digital Image Correlation. *European Journal of Environmental and Civil Engineering* **16**, 1-19.

[27] Pauwels, E., Van Loo, D., Cornillie, P., Brabant, L., and Van Hoorebeke, L. (2013) An exploratory study of contrast agents for soft tissue visualization by means of high resolution X-ray computed tomography imaging, *Journal of Microscopy* **250**, 21-31.

[28] Bannerman, A., Paxton, J. Z. and Grover, L. M. (2013) Imaging the hard/soft tissue interface. *Biotechnology letters* **36**, 1-13

[29] Cantre, D., Herremans, E., Verboven, P., Ampofo-Asiama, J. and Nicolai, B. M. (2014) Characterization of the 3-D microstructure of mango (Mangifera indica L. cv. Carabao) during ripening using X-ray computed microtomography, *Innovative Food Science and Emerging Technologies* **24**, 28-39.

[30] Alba-Tercador, J. (2014) From the sample preparation to the volume rendering images of small animals: A step by step example of a procedure to carry out the micro-CT study of the leafhopper insect Homalodisca vitripennis (Hemiptera: Cicadellidae). *Proceedings of Bruker micro-CT User Meeting,* Ostende, 260-288.

[31] Otani, J., Watanabe, Y. and Chevalier, B. (2010) Introduction of X-ray CT application in geotechnical engineering - theory and practice. *Conference Series: Materials Science and Engineering* **10**, doi: 10.1088/1757-899X/10/1/012089.

[32] Majewski, T., Bobinski, J. and Tejchman, J. FE-analysis of failure behaviour of reinforced concrete columns under eccentric compression. *Engineering Structures* **30**, 300-317, 2008.

[33] Skarżyński, Ł. and Tejchman, J. (2010) Calculations of fracture process zones on meso-scale in notched concrete beams subjected to three-point bending. *European Journal of Mechanics A/Solids* **29**, 746-760.

[34] Marzec, I., Skarżyński, Ł., Bobiński, J. and Tejchman, J. (2013) Modelling reinforced concrete beams under mixed shear - tension failure with different continuous approaches, *Computers and Concrete* **12**, 585-612.

[35] Kozicki, J. and Tejchman, J. (2008) Modelling of fracture processes in concrete using a novel lattice model. *Granular Matter* **10**, 377-388.

[36] Nitka, M. and J. Tejchman, J. Modelling of concrete behaviour in uniaxial compression and tension with DEM. *Granular Matter* **17**, 145-164, 2015.

[37] Tejchman, J. and Bobiński, J. (2013) Continuous and discontinuous modeling of fracture in concrete using FEM. Springer, Berlin-Heidelberg (W. Wu and R. I. Borja, Eds.).

[38] Bažant, Z. P. and Jirasek, M. (2002) Non-local integral formulations of plasticity and damage: survey of progress. *Journal of Engineering Mechanics*, **128**, 1119-1149.

[39] Bobiński, J., Tejchman, J. and Górski, J. (2009) Notched concrete beams under bending - calculations of size effects within stochastic elaso-plasticity with non-local softening. *Archives of Mechanics* **61**, 1-25.

[40] Pijauder-Cabot, G. and Bažant, Z. P. (1987) Non-local damage theory. *ASCE Journal of Engineering Mechanics* **113**, 1512-1533.

[41] Elliott, J. C., Dover, S. D. (1982) X-ray microtomography. *Journal of Microscopy* **126**, 211-213, doi:10.1111/j.1365-2818.1982.tb00376.x.

[42] *http://www.b-cube.ch*

[43] Proudhon, H. (2010) Using X-ray micro-tomography to probe microstructure and damage of structural materials. *WEMESURF contact course*.

[44] Boas, E. and Fleischmann, D. (2012) CT artifacts: Causes and reduction techniques. *Imagining in Medicine* **4**, 229-240.

[45] Skyscan NV (2011) Nrecon User Manual. 4/20/2011.

[46] Landis, E. N., Nagy, E. N., and Keane, D. T. (1997) Microtomographic measurements of internal damage in portland-cement-based composites. *Journal of Aerospace Engineering* **10**, 2-6.

[47] Landis, E. and Nagy, E. (2000) Three-dimensional work of fracture for mortar in compression. *Engineering Fracture Mechanics* **65**, 223-234.

[48] Landis, E., Nagy, E. and Keane, D. (2003) Microstructure and fracture in three dimensions. *Engineering Fracture Mechanics* **70**, 911-925.

[49] Lu, S., Landis, E. N. and Keane, D. T. (2006) X-ray microtomographic studies of pore structure and permeability in Portland cement concrete. *Materials and Structures* **39**, 611-620.

[50] Burlion, N., Bernard, D. and Chen, D. (2006) X-ray microtomography: aplication to microstructure analysis of a cementitious material during leaching process. *Cement and Concrete Research* **36**, 346-357.

[51] Promentilla, M. A. B. and Sugiyama, T. (2010) X-ray microtomography of mortars exposed to freezing-thawing action" *Journal of Advanced Concrete Technology* **8**, 97-111.

[52] Promentilla, M. A. B. and Sugiyama, T. (2011) Microstructure characterization of cement-based materials using X-ray microtomography. *3rd Regional Conference on Chemical Engineering*, Mandaluyong City, Metro Manila.

[53] Łydżba, D., Rajczakowska, M., Stefaniuk, D. and Kmita, A. (2014) Identification of the carbonation zone in concrete using X-Ray microtomography, *Studia Geotechnica et Mechanica* **36**, 47-54.

[54] Skarżyński, Ł, Syroka, E. and Tejchman, J. (2011) Measurements and calculations of the width of fracture process zones on the surface of notched concrete beams. *Strain* **47**, 319-332.

[55] Skarżyński, L. and Tejchman, J. (2013) Experimental investigations of fracture process in plain and reinforced concrete beams under bending. *Strain* **49**, 521-543.

[56] Skarżyński, Ł., Kozicki, J. and Tejchman, J. (2012) Application of DIC technique to concrete - study on objectivity of measured surface displacements. *Experimental Mechanics* **53**, 1545-1559.

[57] Jirasek, M. and Marfia, S. (2005) Non-local damage model based on displacement averaging, *International Journal for Numerical Methods in Engineering* **63**, 77-102.

[58] Peerlings, R. H. J. de Borst, R., Brekelmans, W. A. M. and Geers, M. G. D. (1998) Gradient enhanced damage modelling of concrete fracture. *Mechanics of Cohesive-frictional Materials* **3**, 323-342.

[59] Bobiński, J. and Tejchman, J. (2004) Numerical simulations of localization of deformation in quasi-brittle materials with non-local softening plasticity. *Computers and Concrete* **4**, 433-455.

[60] Le Bellĕgo, C., Dube, J. F., Pijaudier-Cabot, G. and Gerard, B. (2003) Calibration of nonlocal damage model from size effect tests. *European Journal of Mechanics A/Solids* **22**, 33-46.

[62] Ziętkowski, L. (2007). Investigations of splitting of rock and concrete blocks using electro-hydraulic method. *PhD Thesis*. Akademia Górniczo-Hutnicza, Kraków, Poland (in polish).

[62] Scrivener, K.L., Crumbie, A.K. and Laugesen, P. (2004) The interfacial transition zone (ITZ) between cement paste and aggregate in concrete. *Interface Science* **12**, 411-421.

[63] Mondal, P., Shah, S. P. and Marks, L.D. (2009) Nanomechanical properties of interfacial transition zone in concrete. *Nanotechnology in Construction* **3**, 315-320.

[64] Königsberger, M., Pichler, B. and Hellmich, Ch. (2014) Micromechanics of ITZ-aggregate interaction in concrete Part II: strength upscaling. *Journal of American Ceramic Society. Journal of American Ceramic Society* **97**, 543-551.

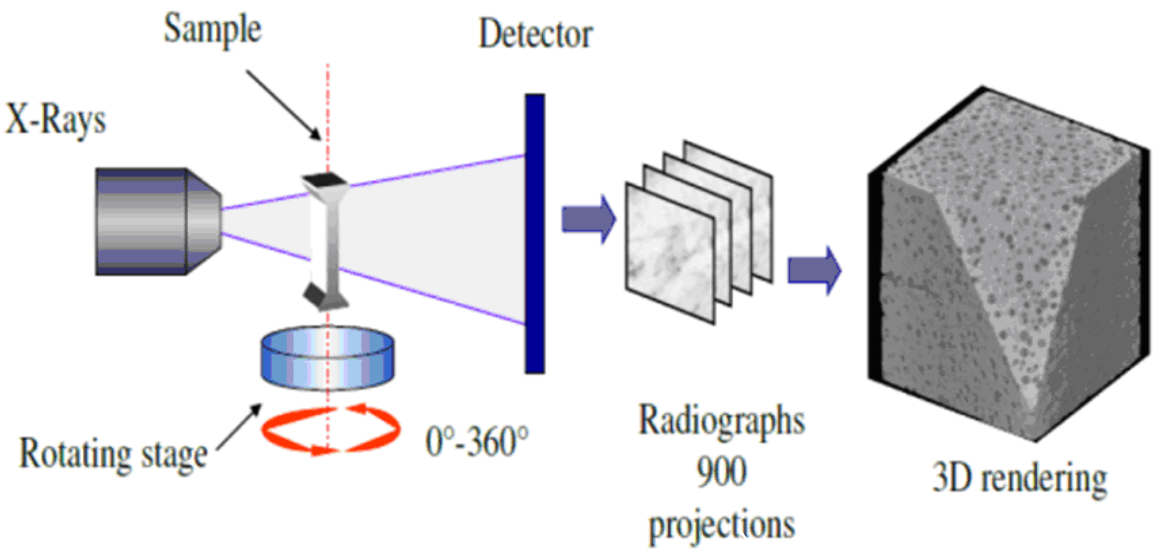

Figure 1: Operation principle of x-ray micro-tomograph [43]

FIGURE 1

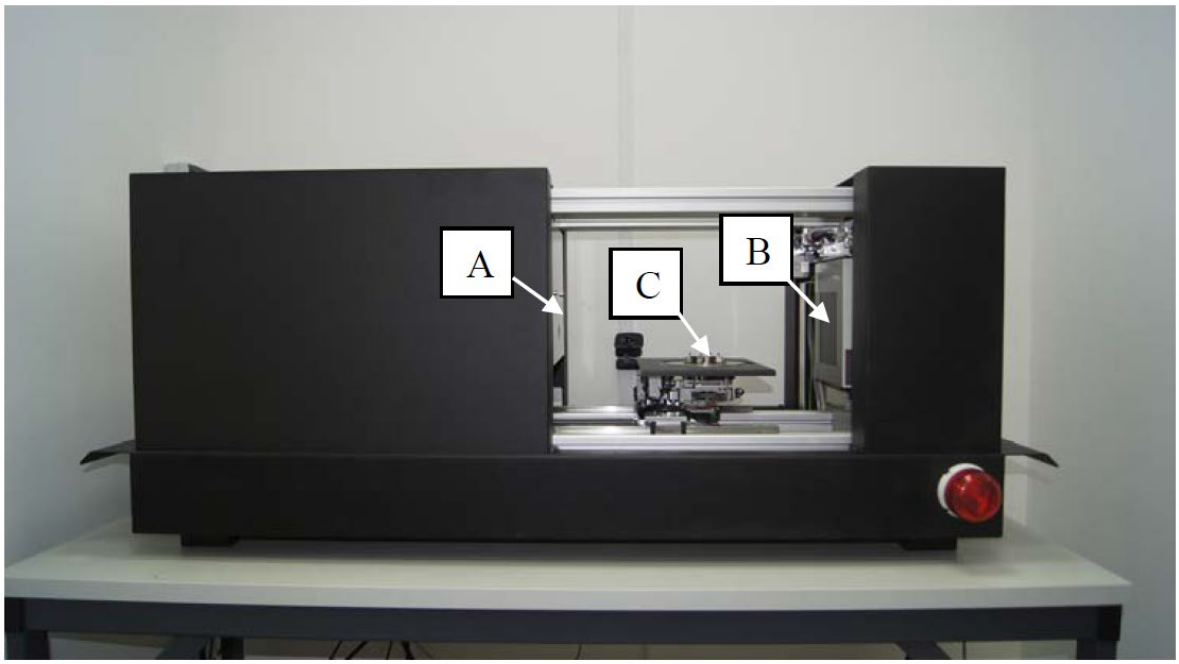

Figure 2: X-ray micro-tomograph by Skyscan 1173: A) x-ray source, B) flat panel and C) precision object manipulator

FIGURE 2

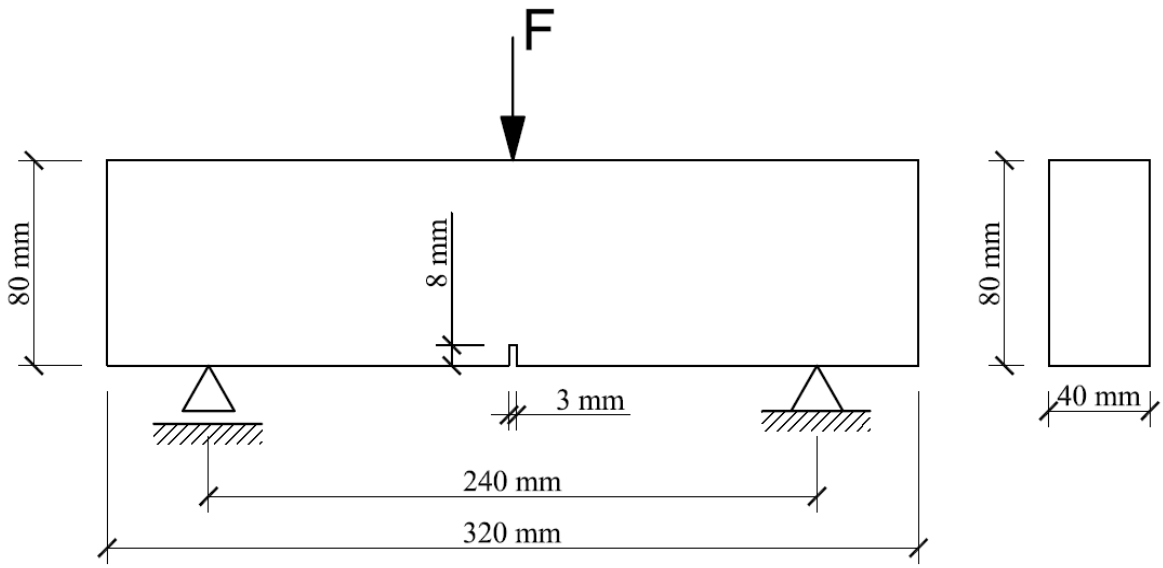

Figure 3: Geometry of experimental concrete beams subjected to three-point bending (*F* - vertical force) [54], [55]

FIGURE 3

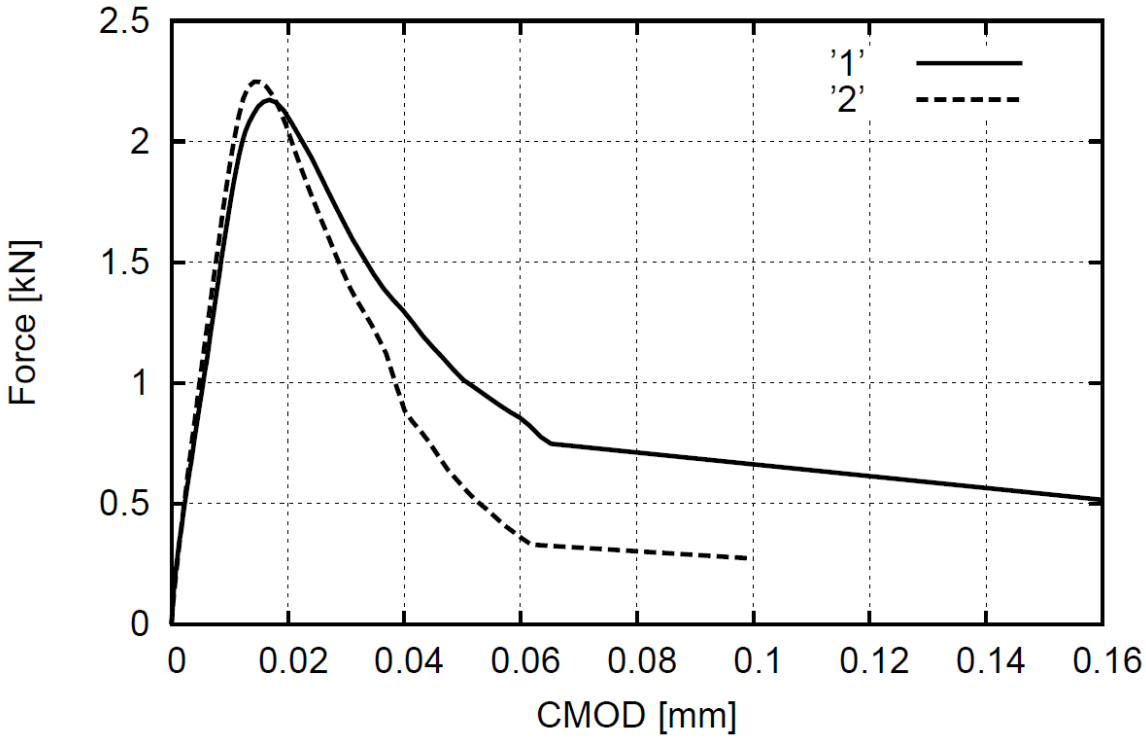

Figure 4: Vertical force-CMOD diagrams from experiments for 2 concrete beams '1' and '2'

FIGURE 4

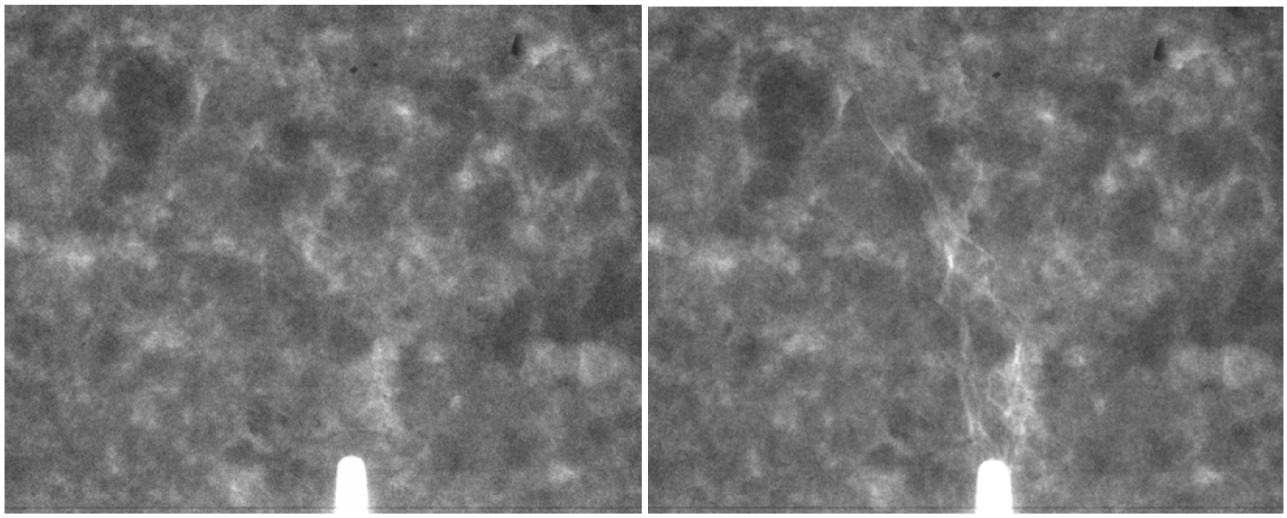

a) b)

Figure 5: 2D X-ray microCT images of concrete beam '2' above notch during deformation process: a) at peak-load and b) in residual state for CMOD=0.1 mm

FIGURE 5

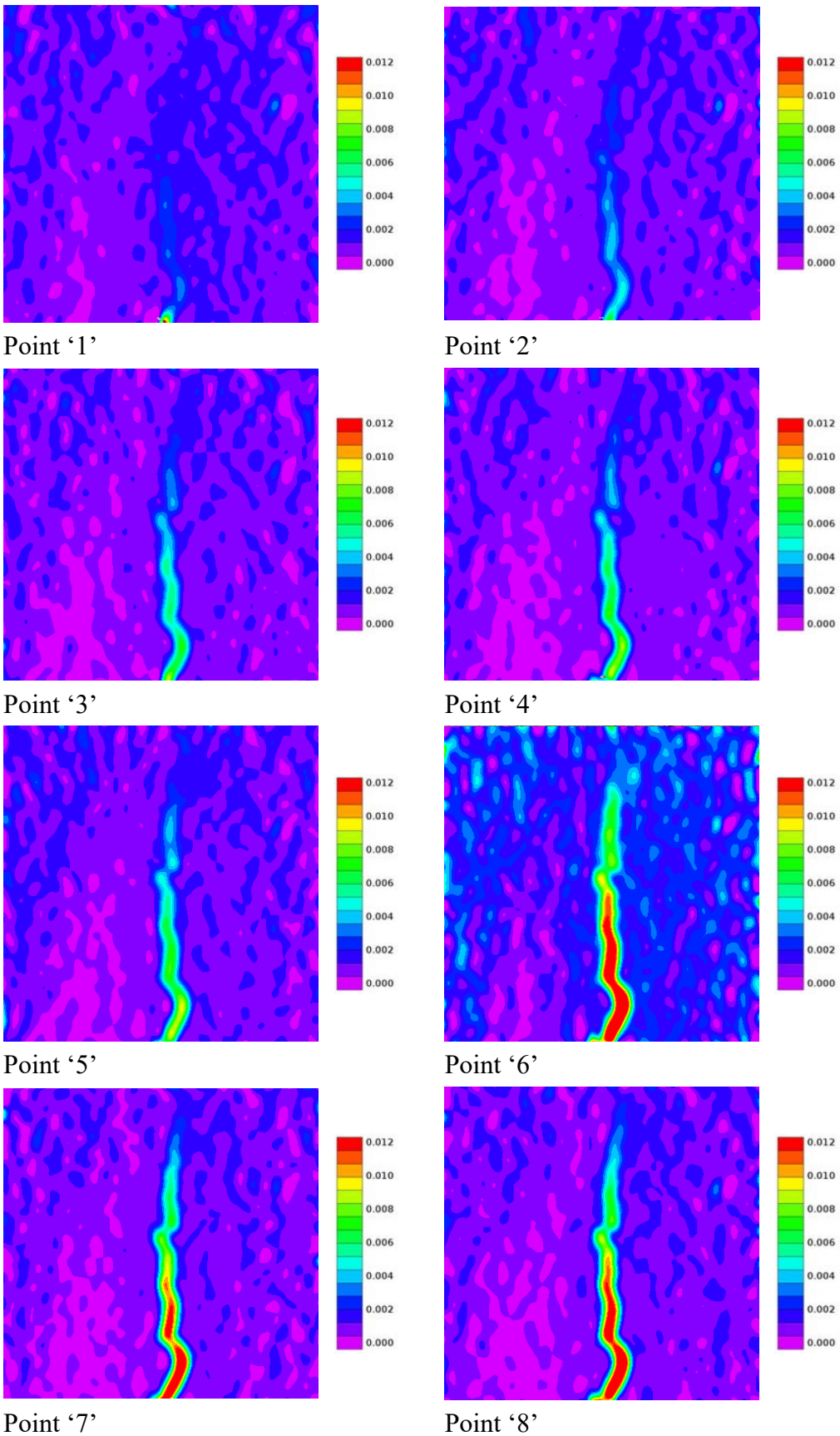

Figure 6: Evolution of fracture process zone directly above notch corresponding to image points of Figure 7 in DIC experiments with beam '1') (single image represents area of 70×70 mm^2, colour scale denotes horizontal normal strain intensity)

FIGURE 6

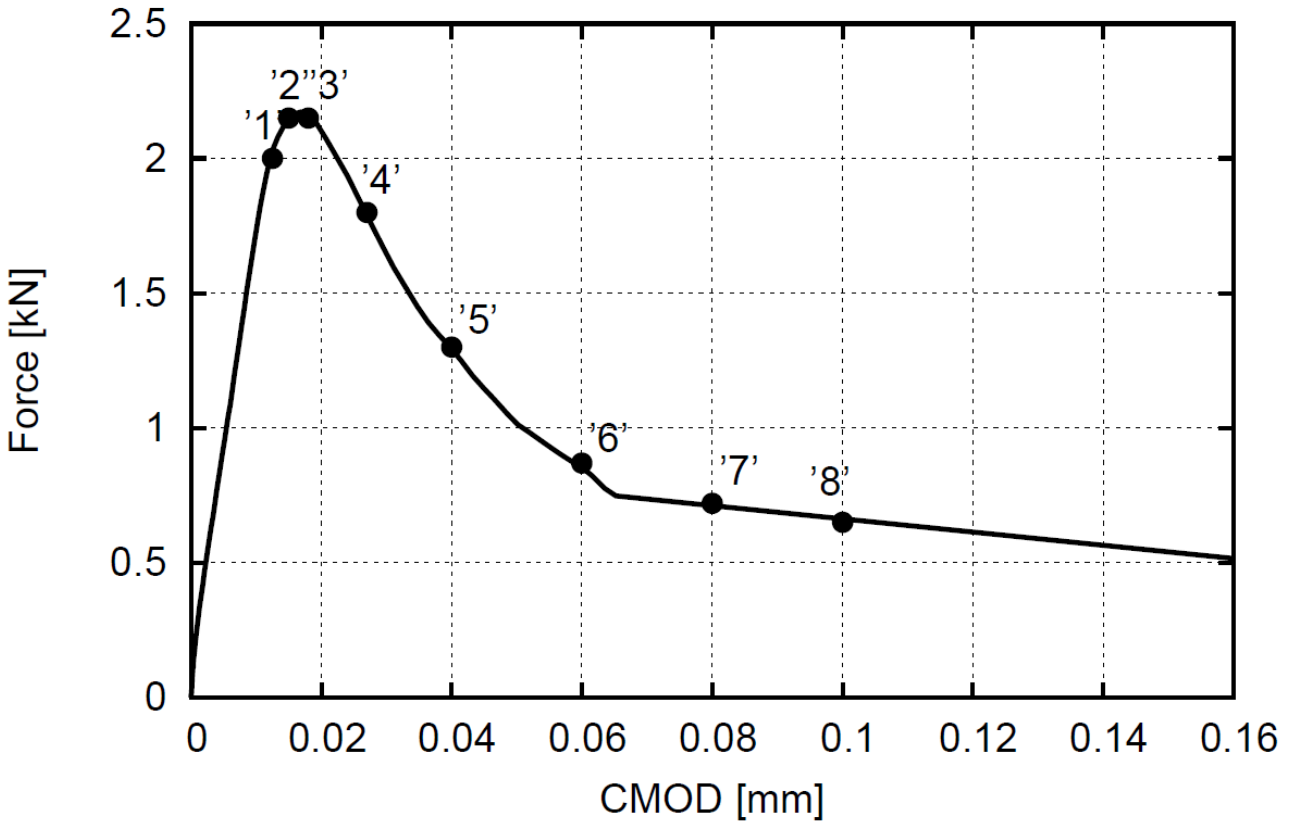

Figure 7: Experimental vertical force-CMOD diagram for concrete beam '1' of Figure 3 with marked points indicating image shot (point '1' indicates moment of localized zone appearance and photo '6' moment of macro-crack onset)

FIGURE 7

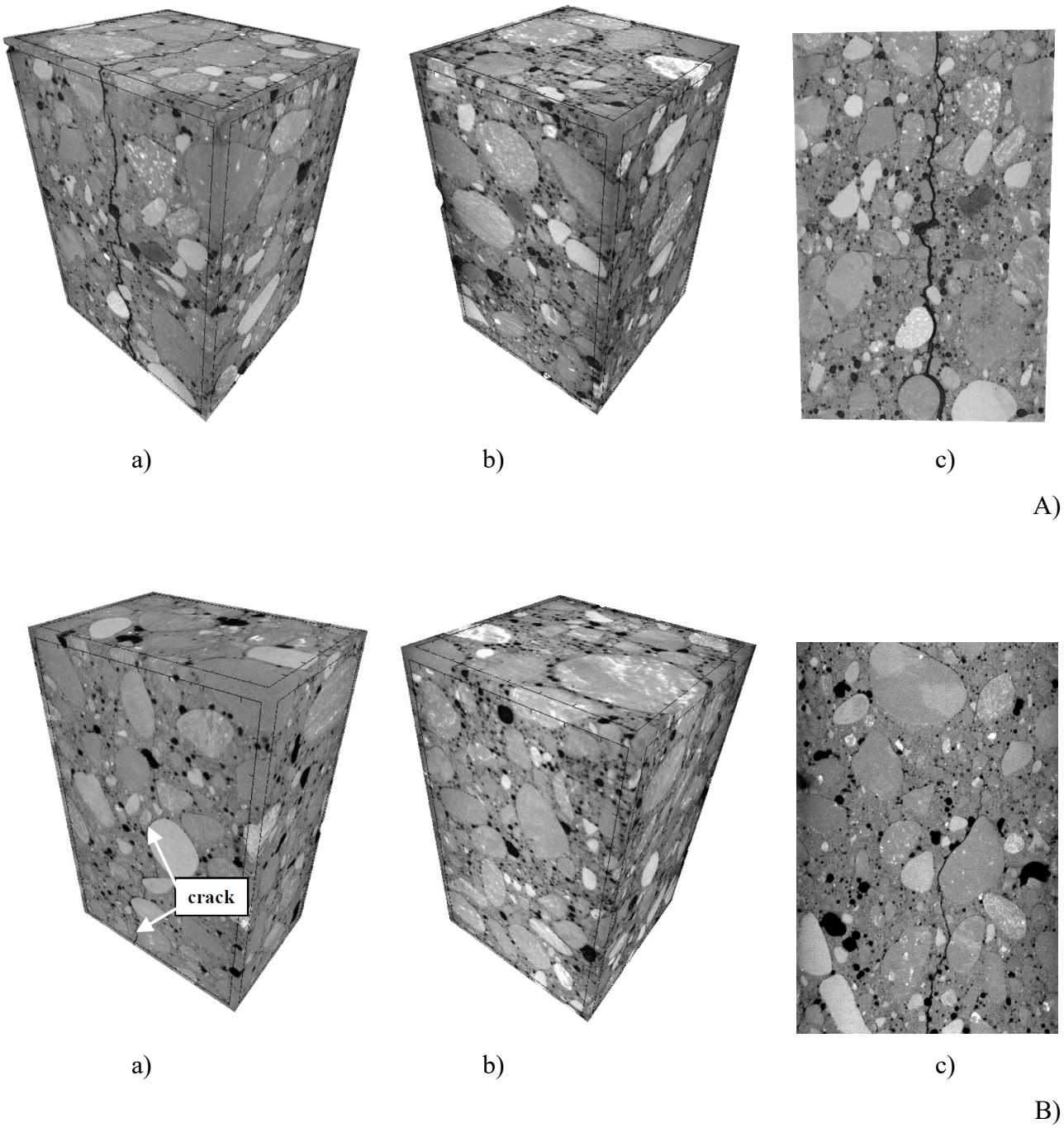

Figure 8: Images of cubical concrete specimens '1' A) and '2' B) 80×40×50 mm^3 by 3D micro-CT): a) cracked specimen after test, b) initially non-cracked specimen and c) cracked specimen front side

FIGURE 8

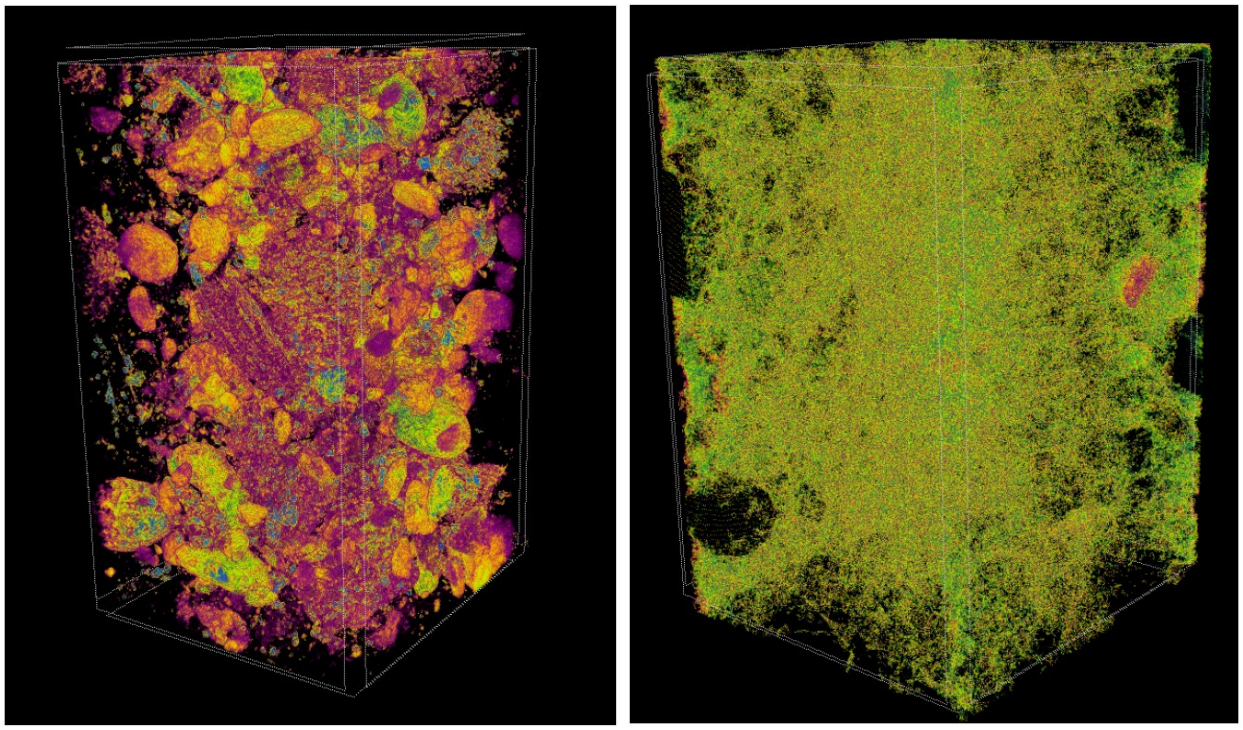

a) b)

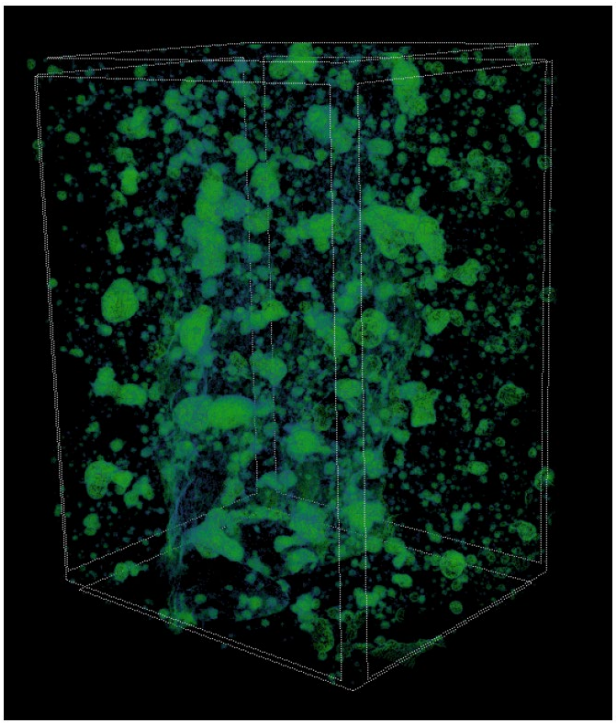

c)

Figure 9: 3D images of cracked cubical concrete specimen '2' by 3D micro-CT with separated phases: a) aggregate particles, b) cement matrix and c) air voids (crack is in blue colour)

FIGURE 9

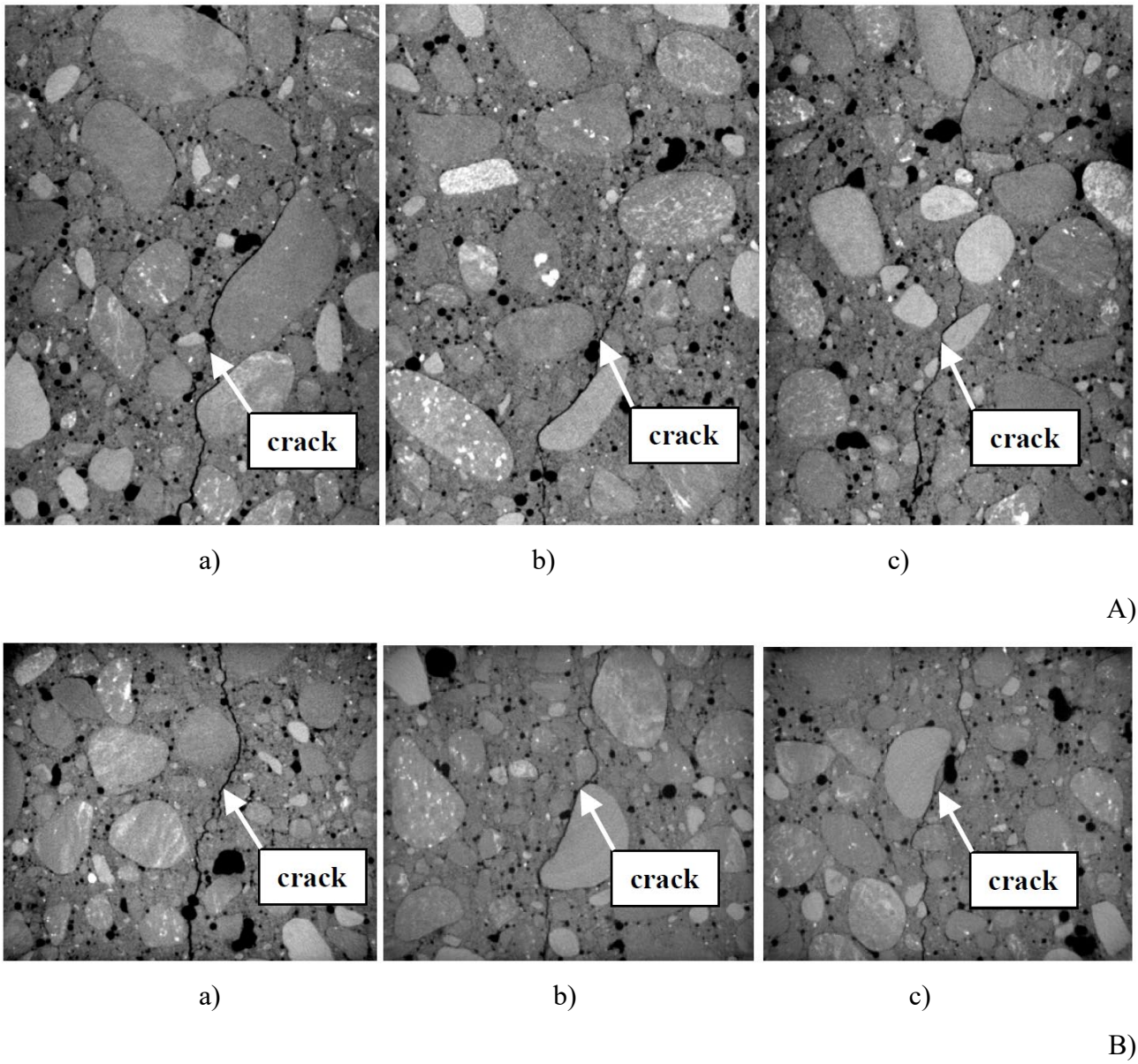

Figure 10: Crack location in cubical concrete specimen 80×40×50 mm^3 of Figure 7Ba after test from 3D micro-CT (concrete specimen '2') in different: A) vertical beam cross-sections (a) at depth of 3 mm, b) at depth of 10 mm (mid-region) and c) at depth 37 mm from front beam surface) and B) horizontal beam cross-sections (a) 3 mm above notch, b) 15 mm above notch and c) 30 mm above notch)

FIGURE 10

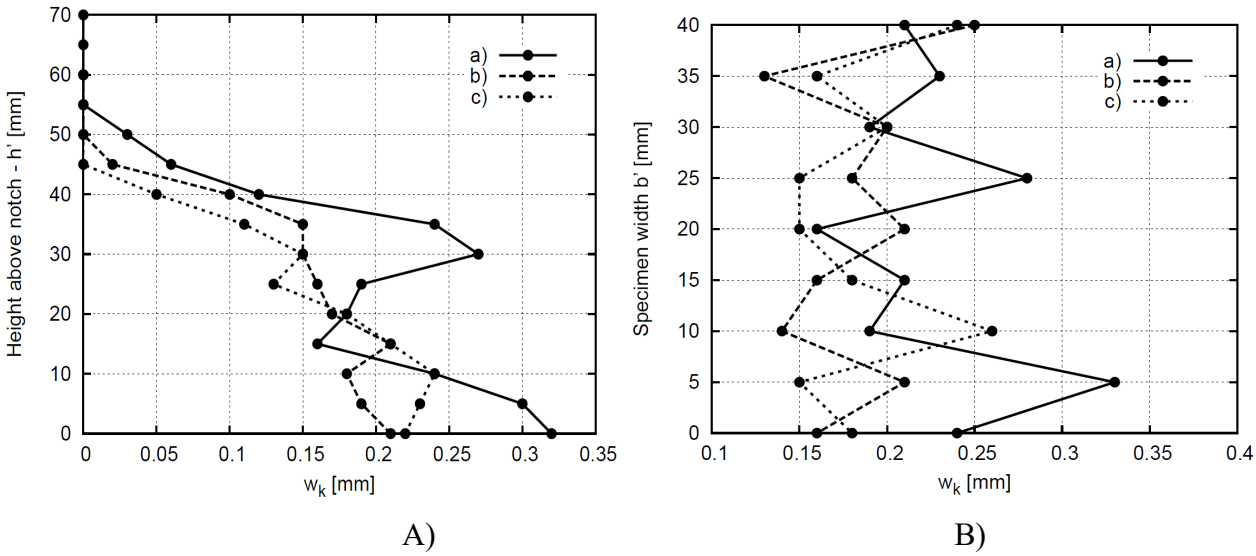

Figure 11: Width of crack in concrete specimen '2': A) in 3 vertical cross-sections and B) in 3 horizontal cross-sections of Figure 10

FIGURE 11

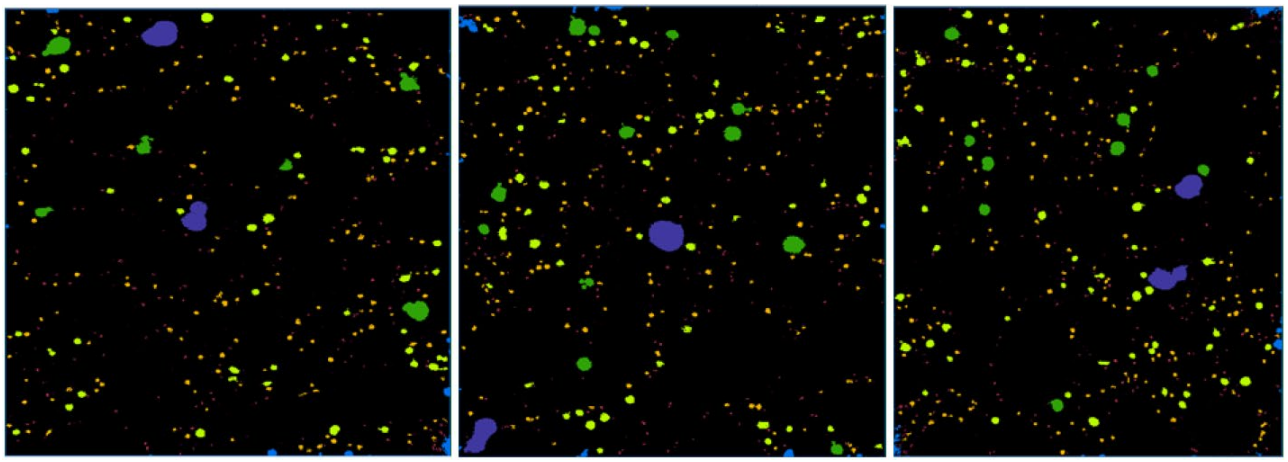

a) b) c)

A)

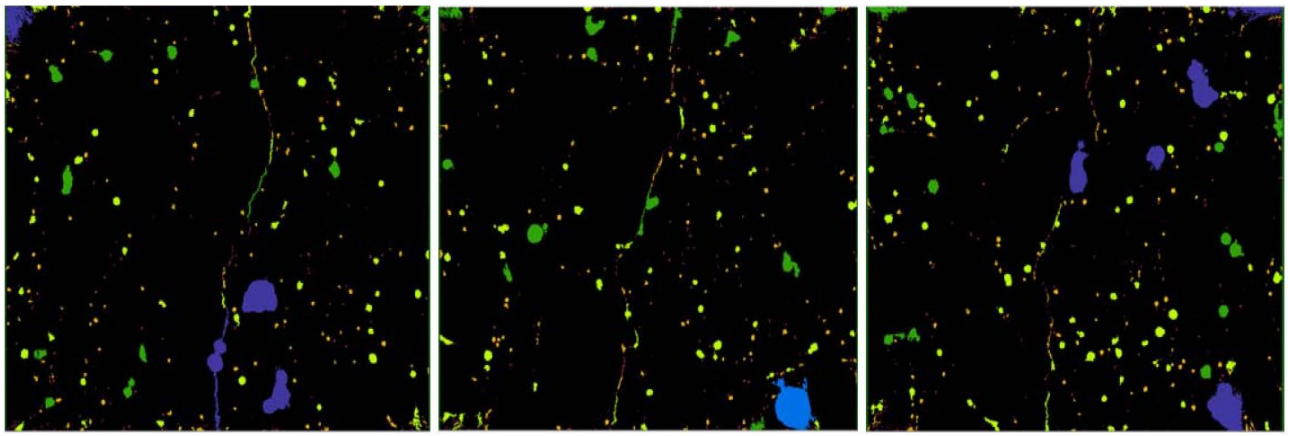

a) b) c)

B)

Figure 12: Images of air voids in different horizontal cross-sections 40×50 mm^3 above beam notch of non-cracked (A) and cracked (B) concrete specimen '2' of Figure 8B a) 5 mm above notch, b) 15 mm above notch and c) 30 mm above notch (colours stand for air voids with different diameter)

FIGURE 12

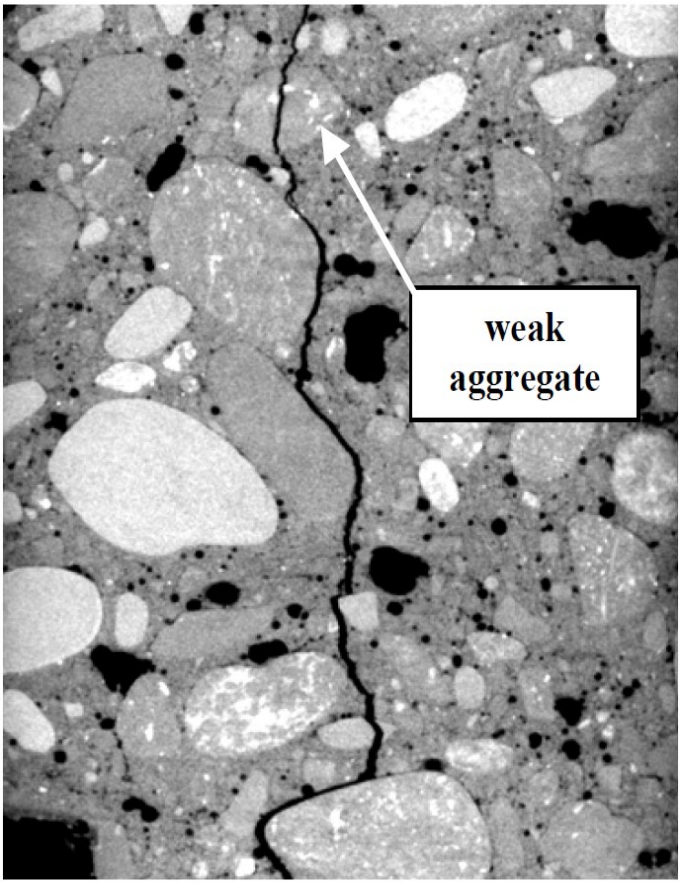

Figure 13: Crack propagation along beam height through single aggregate particle (concrete specimen '1')

FIGURE 13

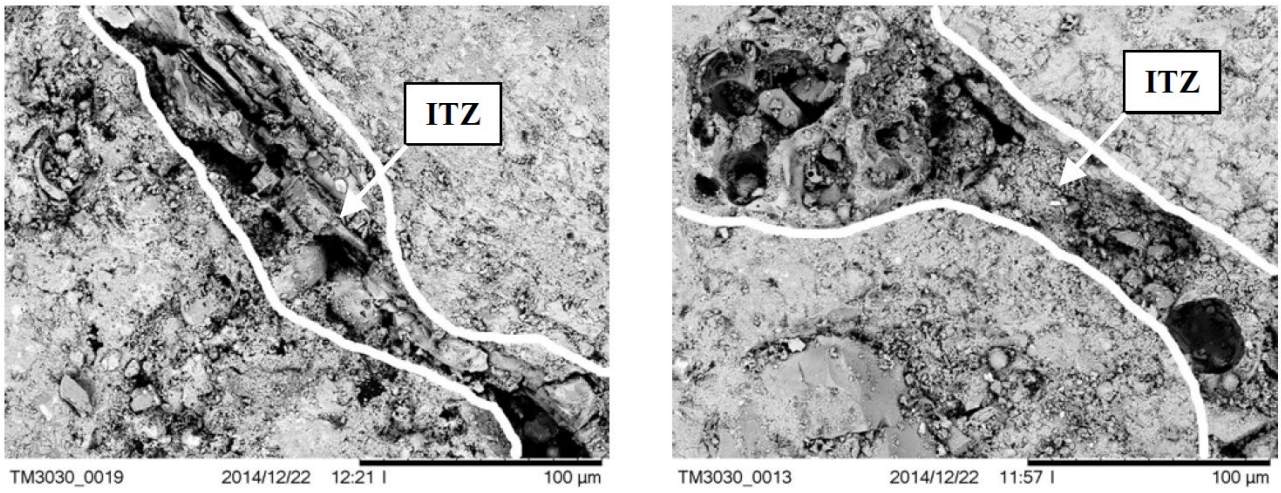

Figure 14: Images of ITZs by scanning electron microscope (SEM) (porous zones close to aggregate represent ITZs)

FIGURE 14

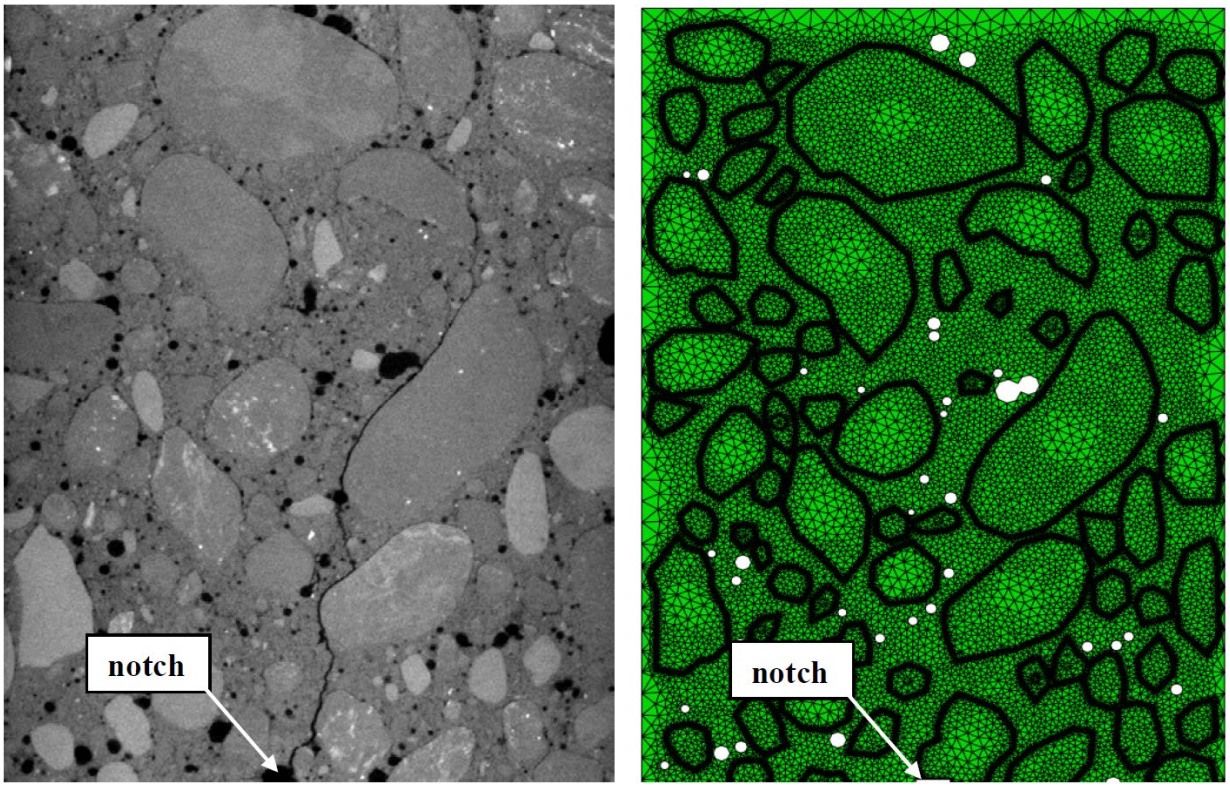

a) b)

Figure 15: Micro-structure of concrete specimen of Figure 8B in the region of notch: a) initial image at depth of 3 mm from front side of concrete beam '2' by micro-CT and b) FE mesh assumed for concrete as 4-phase random heterogeneous material

FIGURE 15

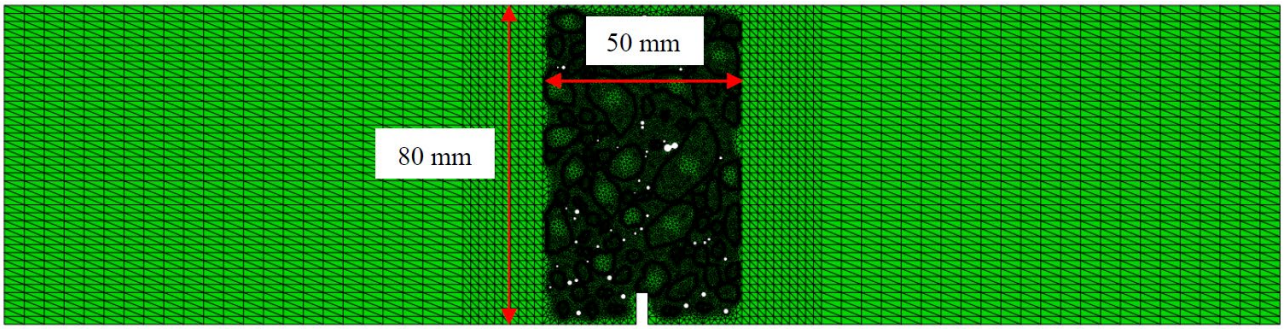

Figure 16: 2D FE mesh for entire beam '2' with meso-region of 50×80 mm^2

FIGURE 16

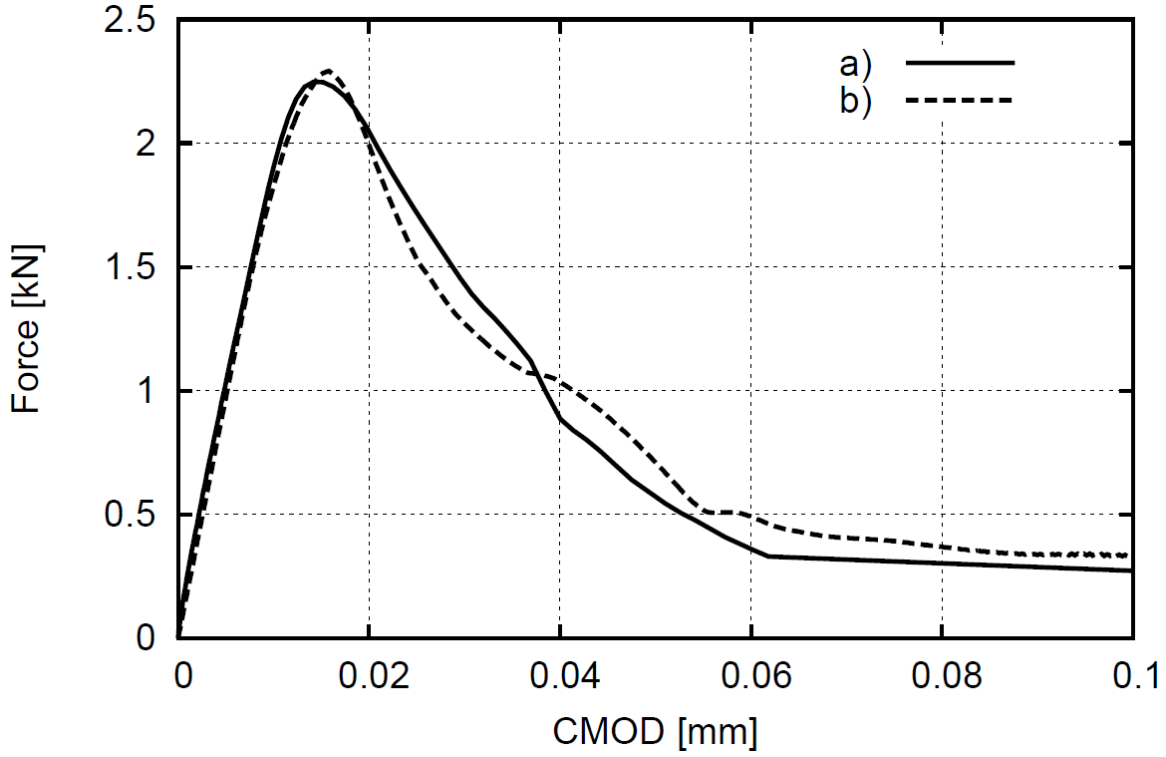

Figure 17: Diagram of vertical force against CMOD from: a) experiments and b) FE computations (concrete beam '2')

FIGURE 17

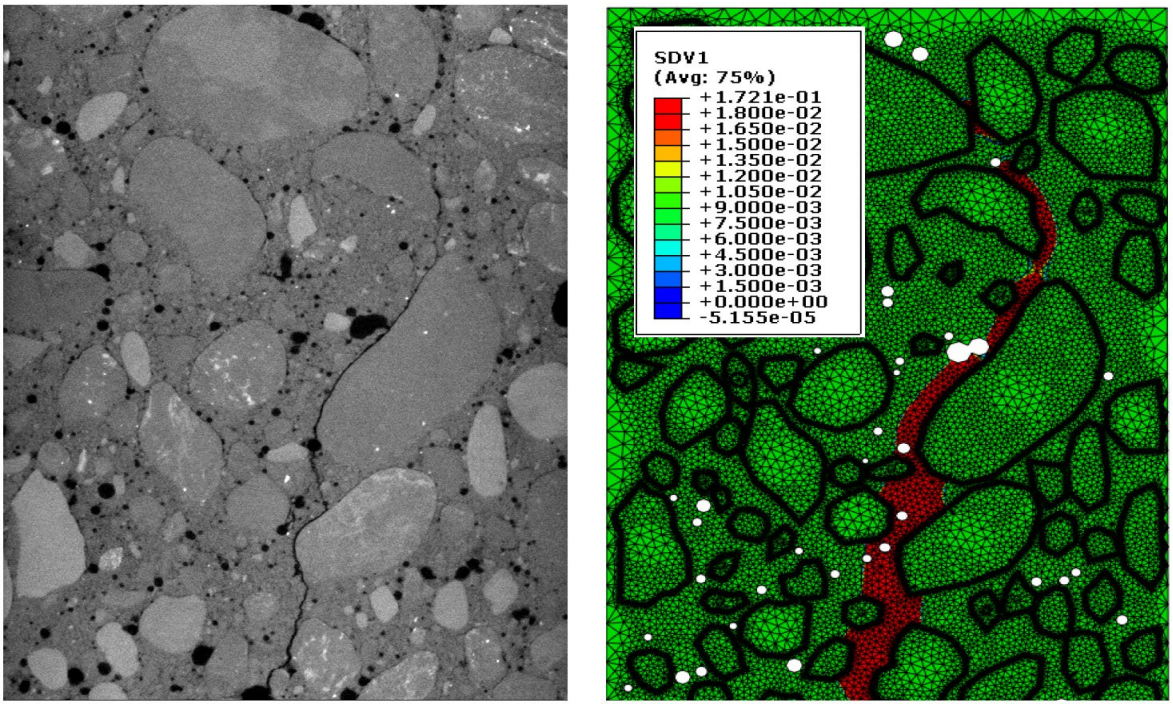

a) b)

Figure 18: Comparison between experiments and FE analyses (concrete beam '2'): a) image at depth of 3 mm from front side of concrete beam '2' by micro-CT after test (CMOD=0.1 mm) and b) calculated distribution of non-local strain measure above notch in residual state (CMOD=0.1 mm)

FIGURE 18

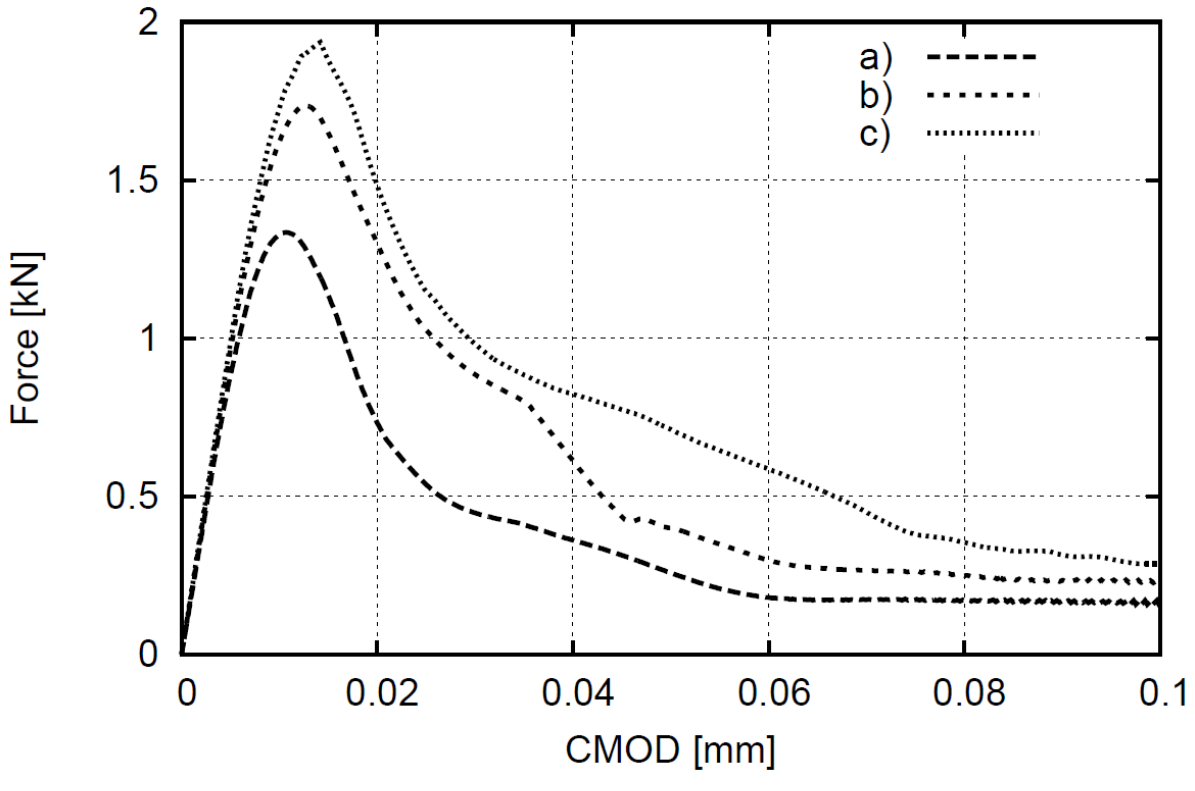

A)

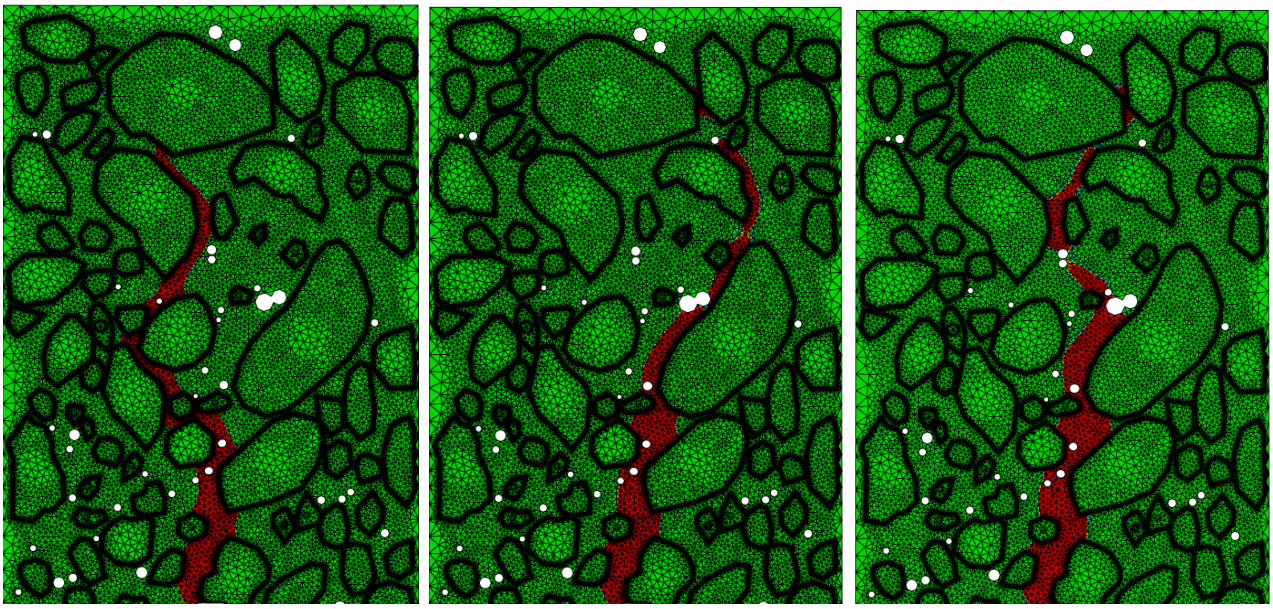

a) b) c)

B)

Figure 19: Effect of different elastic modulus of ITZs E^{ITZ} on force-CMOD diagram (A) and localized zone for CMOD=0.1 mm (B) in FE analyses: a) E^{ITZ}=7.3 GPa, b) E^{ITZ}=14.6 GPa and c) E^{ITZ}=21.9 GPa, characteristic length of micro-structure l_c^m=1.5 mm and crack initiation strain $\kappa_0^{\mathrm{ITZ}}=4.0\times10^{-5}$)

FIGURE 19

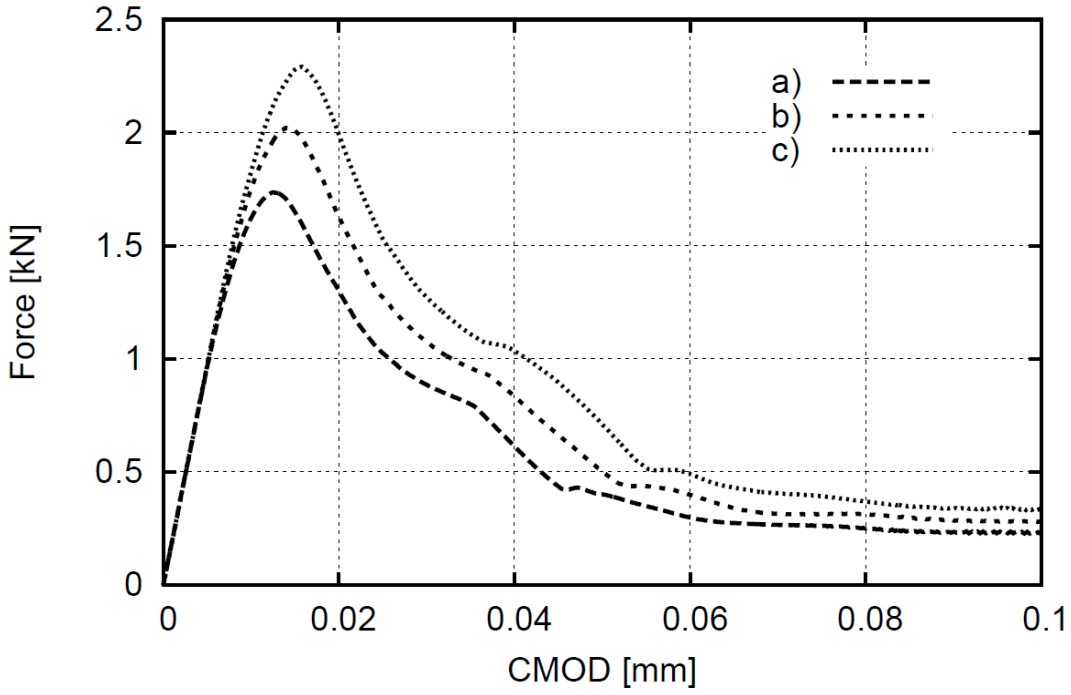

Figure 20: Effect of different crack initiation strain κ_0 in ITZs on force-CMOD curve in FE analyses: $\kappa_0^{ITZ}=4.0\times10^{-5}$, b) $\kappa_0^{ITZ}=7.5\times10^{-5}$ and c) $\kappa_0^{ITZ}=1.1\times10^{-5}$, characteristic length of micro-structure $l_c^m=1.5$ mm and elastic modulus $E^{ITZ}=14.6$ GPa)

FIGURE 20

LIST OF TABLES

Table 1: Concrete mix used in experiments (d_{50} - mean aggregate diameter, d_{max} - maximum aggregate diameter, β - aggregate volume)

Concrete components	**Concrete mix** (d_{50}=2 mm, d_{max}=16 mm, β=75%)
cement (Portland 32.5R)	810 kg/m^3
sand (0 - 2 mm)	650 kg/m^3
gravel aggregate (2 - 8 mm)	580 kg/m^3
gravel aggregate (8 - 16 mm)	580 kg/m^3
water	340 kg/m^3

Table 2: Crack length, width and area measured in concrete specimen '2' with x-ray micro-tomograph

(^{v} - value in vertical cross-section, ^{h} - value in horizontal cross-section)

Cross-section	**Crack length [mm]**	**Crack area [mm^2]**	**Average crack width [mm]**
Figure 10Aa	59.31^v	14.23^v	0.24^v
Figure 10Ab	53.85^v	10.77^v	0.20^v
Figure 10Ac	51.19^v	9.73^v	0.19^v
Figure 10Ba	43.08^h	11.21^h	0.26^h
Figure 10Bb	45.09^h	10.41^h	0.22^h
Figure 10Bc	44.29^h	7.97^h	0.18^h

Table 3: Void area and void size in horizontal cross-sections of concrete specimen '2' (Figure 13A)

Cross section	Void area [mm^2]	Percentage void area [%]	Diameter range for each void size [%]				
			0.13-0.25 mm	0.25-0.51 mm	0.51-1.02 mm	1.02-2.03 mm	2.03-4.06 mm
Figure 16a	76.59	4.58	8.52	19.78	31.25	24.97	14.06
Figure 16b	89.33	5.28	8.53	21.99	27.56	25.67	16.25
Figure 16c	84.88	5.02	9.79	22.46	31.57	19.54	16.64

Table 4: Material constants assumed in FE calculations of concrete beam on meso-scale

Parameter	Aggregate	Cement matrix	ITZ
Modulus of elasticity E [GPa]	47.2	29.2	14.6
Poisson's ratio υ [-]	0.2	0.2	0.2
Crack initiation strain κ_0 [-]	-	1.5×10^{-4}	1.1×10^{-4}
Residual stress level α [-]	-	0.95	0.95
Slope of softening β [-]	-	200	200